CHAPTER VI
Analysis of more galaxies

The detailed analysis of NGC 4254 has proven the overall feasibility of the approach. It showed that the gas contribution in galaxies can be modelled to a high enough precision to enable the comparison to real measured data and to draw valuable conclusions. However, the agreement between the simulated and the measured gas velocity field was only partly satisfactory on a wiggle-to-wiggle basis. Further, the analysis of a single galaxy could not provide any insight, whether the result is characteristic for luminous, non-barred spirals as a whole. The extension of the analysis on a sample of galaxies might promise a better comprehension of the relevant gas processes in spiral galaxies, leading to a more reliable and representative estimate of the dark matter content and distribution.

The analysis was applied to the rest of the galaxies from the sample, for which sufficient kinematic data could be taken and optical photometry was available, hence the color correction could be performed. This applied to four more galaxies: NGC 3810, NGC 3893, NGC 5676 and NGC 6643 as listed in Tables 4.1 and 4.2. NGC 5364 was not included, since only 5 slit positions could be taken, providing only a relatively poor guess of the two-dimensional velocity field.

The modelling of the gravitational potentials followed the procedure that was outlined in Chapter 4. Only where a differing, individual treatment was needed for single galaxies modelling issues will be described further in this Chapter. For all galaxies a large set of simulations was performed for a wide range of the spiral pattern speeds. Furthermore, following the example of NGC 4254, simulations were carried out for five different mass fractions of the stellar disk, namely $f_d = 20\,\%, 45\,\%, 60\,\%, 85\,\%$ and a maximal disk. Since it became evident from the analysis of NGC 4254 that the choice of the gas sound speed affects the conclusions only at unphysically high values for c_s, all further simulations were performed assuming a sound speed $c_s = 10\,\mathrm{km\,s^{-1}}$. To account for the uniqueness of each galaxy, this Chapter is divided into Sections describing the simulations and results for each galaxy separately.

6.1. NGC 3810

NGC 3810 is a relatively bright Sc galaxy located in the Leo group of galaxies. It exhibits a fairly strong two-arm morphology with an arm to inter-arm contrast of $0.45 - 0.75$ mag in K'. At radii larger than $\approx 45''$ the two arm structure gradually fades into a more fragmented or flocculent structure (see Figure 6.1). The flocculence of NGC 3810 is even

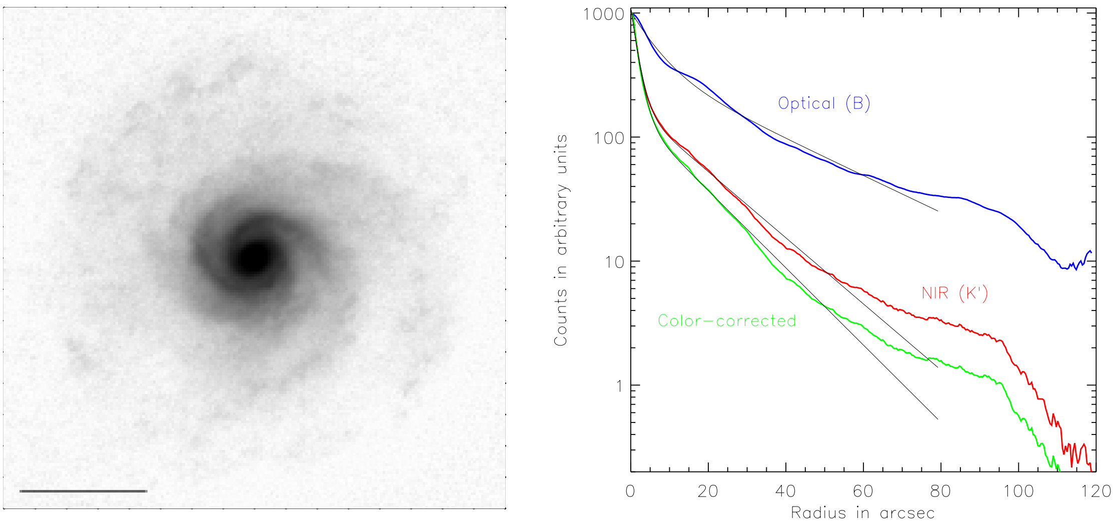

Figure 6.1 NGC 3810. At left the deprojected, color-corrected, H II-region cleaned image of NGC 3810 is shown. It was used as an input to calculate the gravitational potential of the stellar disk contribution to the total gravitational potential. The scaling bar is $1'$. At right, the effect of the color correction on the disk scale length of NGC 3810 is shown. Note the deviation of the azimuthally averaged radial light profiles from a simple exponential. The fitted part (black lines) of the color corrected profile steepens by 14.7 %, as compared to the K-band.

more apparent in the visible, and is seen best in the 'Color Atlas of Galaxies' (Wray 1988). In a study of the NIR appearance of flocculent galaxies Elmegreen et al. (1999) argue that the flocculent optical appearance might be caused by higher than usual dust extinction between the arm pieces. Indeed, dust might play a role, but most probably not the most important, since 10 out of their sample of 14 galaxies kept their flocculent appearance also in the NIR. Elmegreen et al. (1999) further note that the arms of NGC 3810 are reasonably well matched by logarithmic spirals, however, they find a break in mid-disk, where emerging arms have a higher pitch angle than the main arms, perhaps evidence for a spur (Elmegreen 1980). This flocculent part of the disk has a rather constant surface brightness of ≈ 21 mag per square arcsecond. Beyond about $100''$ the surface brightness drops steeply until reaching the exponential decline of the inner disk at about a radius of $115''$ (see Figure 6.1). A distance of 13.5 Mpc was assumed towards NGC 3810, taken as an average literature value. At this distance the galaxy's a K-band exponential scale length of $16''.3$ corresponds to 1.07 kpc; although the profile is not entirely exponential. This is the shortest scale length of all 5 galaxies in the sample. NGC 3810 has a total blue magnitude of $B_T = 11.3$ mag and the bright part of the disk measures 3.4×2.4 arcminutes on the sky. The major axis position angle, PA $= 22^\circ.0$, and the inclination of the disk, $i = 46^\circ.0$, were determined from the measured kinematics. The inclination corrected rotation curve rises gently and flattens at a radius of about $40''$ to a constant value of $150\,\mathrm{km\,s^{-1}}$. There is no evidence for a bar at the center.

The color correction leaves the overall morphology of NGC 3810 basically unchanged. There seem no large arm-to-arm population differences that cause the spiral structure to change drastically. However, the color correction causes the radial profile to become

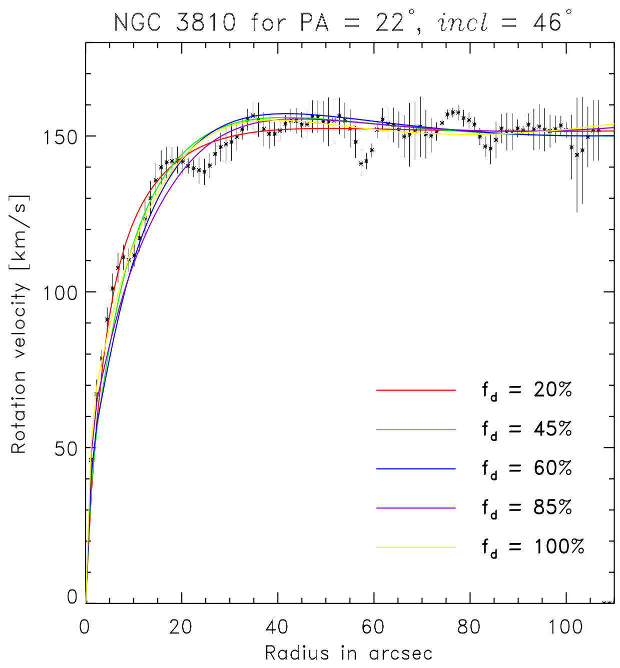

Halo parameters

f_d [%]	R_{core} [kpc]	v_∞ [$km\,s^{-1}$]
20	0.23	168
45	0.39	150
60	0.62	139
85	1.74	141
100	3.06	149

Figure 6.2 Rotation curve comparison for NGC 3810. The five axisymmetric model potentials for different fractions of the stellar disk potential yield rotation curves that are very similar and match well with the observed kinematics.

steeper by 14.7 %, the largest change from a color correction in any of the sample galaxies (see Figure 6.1 and Table 4.2).

Five models of the total gravitational potential were prepared for NGC 3810, varying the stellar disk mass fraction f_d. Figure 6.2 shows the rotation curves from the five axisymmetric model potentials, as compared to the observed kinematics. All model rotation curves can explain the galaxy's observed rotation curve similarly well. The Table accompanying Figure 6.2 lists the core radii and asymptotic rotation velocities of the five pseudo-isothermal halo models used to assemble the final galaxy potentials.

6.1.1. Performing the hydrodynamical gas simulations

To model the two-dimensional gas surface densities and velocity fields for NGC 3810 a set of simulations was carried out on a 201×201 Cartesian grid. The grid cells were chosen to give a resolution of 77.76 pc per cell for the assumed distance towards the galaxy of 13.5 Mpc. As for NGC 4254 the gas is taken to be isothermal throughout the simulation, implying that the gas cools instantaneously to its initial temperature during each updating timestep. Following the initialization of the gas in centrifugal balance in an axisymmetric potential, the final non-axisymmetric potential is gradually turned on and the simulation is completing the initialization phase by the time 40 sound crossing times of the code have passed. For NGC 3810, assuming a gas sound speed $c_s = 10\,km\,s^{-1}$, that occurs after about 436 Myrs.

To find the spiral pattern speed Ω_p, or equivalently the corotation radius R_{CR}, the following cases were modelled: $R_{CR} = 3.15$, 3.43, 5.04, 6.14, 6.45, 7.00, 7.79, 10.0 kpc and no pattern rotation. For the different stellar disk mass fractions f_d not all of the above listed corotation radii were simulated. Table 6.1 provides an overview of the runs which were performed for NGC 3810.

Table 6.1 Hydrodynamic simulations for NGC 3810. Given is the duration of the individual simulation in units of 10^6 years.

f_d	corotation radius R_{CR} [kpc]								
[%]	3.15	3.43	5.04	6.14	6.45	7.00	7.79	10.0	∞
20	1302	1302	1302	1302	1302	1302	1302	1302	—
45	1302	1302	882	1222	1282	1042	—	—	—
60	602	862	642	722	802	942	1002	1302	1302
85	702	421*	562	702	782	582	—	—	—
100	441	441	522	742	762	502	—	—	—

* Note: This run terminated before ending the initialization phase of the simulation, which occurs at 436 Myrs.

6.1.2. Premature termination of simulations

As apparent from Table 6.1 some of the simulations, especially the ones for a fast pattern rotation (small R_{CR}) and high disk mass fractions, terminated before the simulation reached the anticipated run time of 1302 Myrs. For one run, the simulation terminated even before the full non-axisymmetric galaxy potential was turned on. In such a case, problems occur at certain grid cells during the simulation. Usually the gas density in the particular grid cell becomes very low, implying conditions that are at the limit of the code's range of application. For treating the gas flows in disk galaxies on a Cartesian grid, high order interpolations have to be applied. In extreme situations, they cause the code to produce unphysical negative gas density values for the next updating time step. Repeated occurrence of this problem eventually causes the simulation to stop. The occurrence of these negative densities is aggravated by various processes. First, in the central regions the gas density contrast can get very high, triggered by the non-axisymmetric nature of the potential. Second, these conditions become more severe, if the potential has a higher degree of non-axisymmetry, i.e. for the $f_d = 85$ and 100 % cases. Third, if the pattern rotation is high, shocks tend to become stronger since the gas is exposed to faster potential changes. Finally, for massive galaxies with high rotation velocities in the disk the velocity gradient in the inner parts of the disk is very large. Eventually, one of these processes, or a combination of them, might produce such extremely rarefied gas conditions in a grid cell, terminating the simulation prematurely.

If the parameters for a simulation are close to the ones yielding the best representation of the galaxy properties the χ^2/N comparison between the simulated gas kinematics and the observations retains a very constant value, once the simulation proceeded past its initialization phase. This is demonstrated in Figure 6.3. The χ^2/N value fluctuates at maximum on a few-percent level. Thus, the evaluation of any simulation timestep past the initialization phase can be regarded as being equivalent. For the data analysis, a mean is calculated. The median of the χ^2 exhibits a very similar behavior. However, if the parameters for a simulation are far from representing a good description of the modelled galaxy, the simulation might not reach a stationary solution and the χ^2/N value increases without limits. Often in these cases the simulation terminates prematurely. An example is displayed in Figure 6.4.

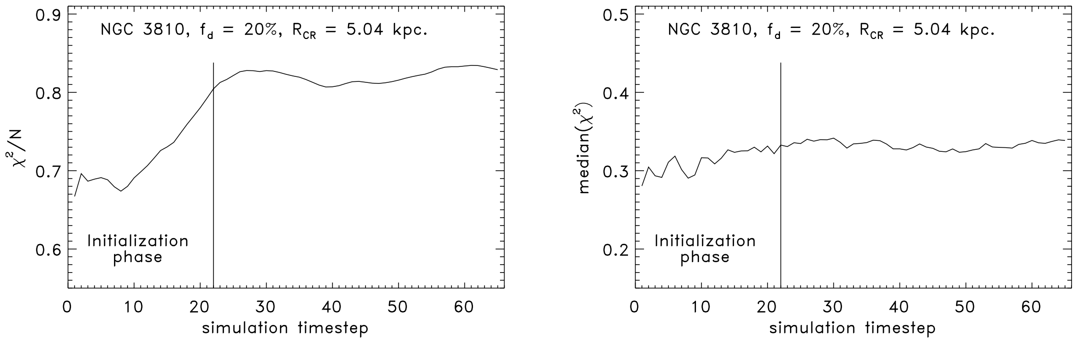

Figure 6.3 The overall χ^2/N-value and the median(χ^2) of the model-to-observed kinematics comparison, plotted for a successful simulation of NGC 3810. The full non-axisymmetric potential is turned on at timestep 22. χ^2/N is quite stable after the initialization phase as well as the median(χ^2).

Any simulation that terminated before the full non-axisymmetric potential was fully turned on will give χ^2-values that are slightly off. In general these simulations tend to give lower χ^2s than what would be expected if the simulation had continued to the end. In the further analysis, some results of prematurely terminated simulations are included into the discussion, but they are always marked as being less reliable.

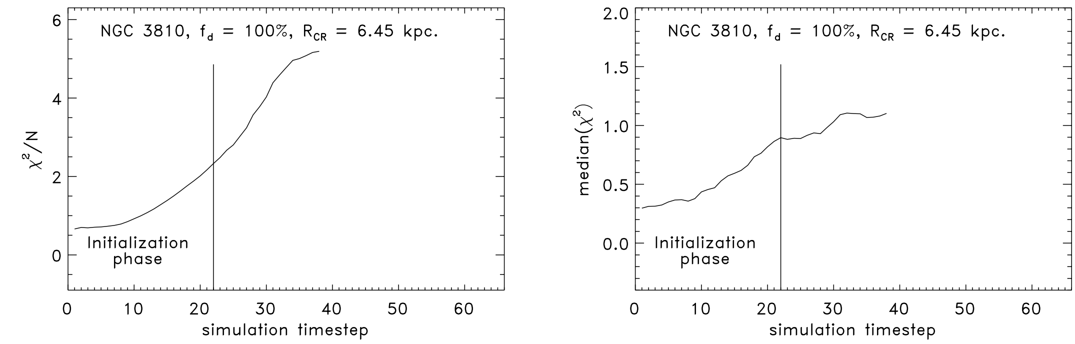

Figure 6.4 The overall χ^2/N-value and the median(χ^2) of the model-to-observed kinematics comparison, plotted for a terminated simulation of NGC 3810. The full non-axisymmetric potential is turned on at timestep 22. χ^2/N does not reach a stationary value after the simulation proceeded past its initialization phase. The median(χ^2) follows the same trend, although less vigorous. Note the different scales on the χ^2-axis.

6.1.3. Results from the hydrodynamical gas simulations

6.1.3.1. The gas density

NGC 3810 has a disk with a two-fold morphology. In fact, only the inner disk reveals a fairly strong spiral structure. In the outer disk no well defined high contrast arms can be found. In the simulation for the best matching corotation radius (Figure 6.5), primarily the inner spiral determines the degree of how well observations and simulations agree. The simulated gas density exhibits a fairly regular 3-arm morphology, that splits into several pieces before it almost dissolves at the corotation radius. The simulations trace quite well the underlying spiral structure, putting the strongest gas shocks to where the spiral arms are best defined and most of the star forming H II-regions are located. Beyond corotation the simulation develops long and continuous shocks that form in response of the weak outer spiral pattern. These shocks come to lie close to where the arms are. Thus, the overall agreement between the simulated gas density morphology and the galaxy's spiral pattern is good.

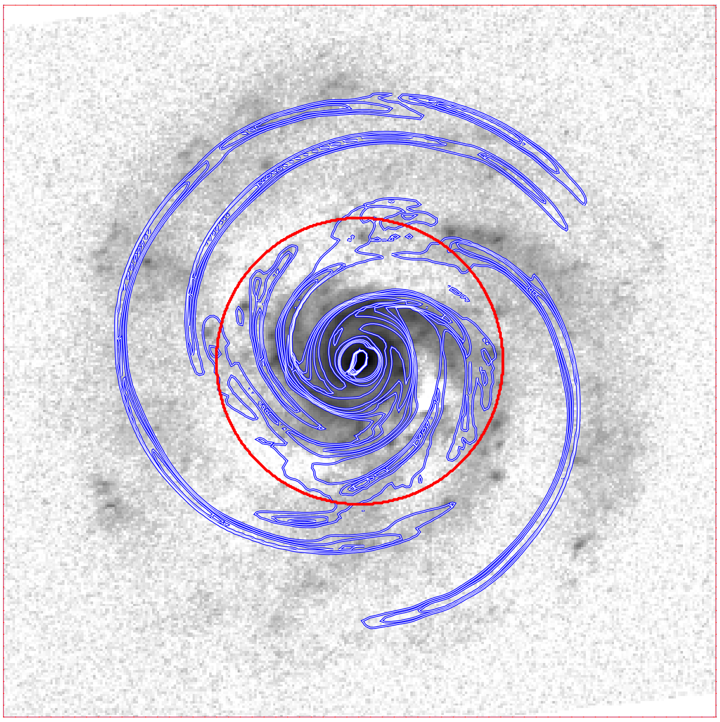

Figure 6.5 Simulation results of the gas density distribution overlaid in contours onto the deprojected K'-band image of NGC 3810. From the image an axisymmetric radial brightness profile has been subtracted to enhance the contrast of the spiral arms. The Figure shows the contours for the simulation with $\mathrm{f_d} = 60\,\%$ and a corotation radius (red circle) of 3.15 kpc. The full set of simulation results is shown in Appendix A.

NGC 3810 appears to be a galaxy with a fast pattern rotation. The simulations resulting in a gas density pattern that resembles the observed spiral morphology the most were the ones with the smallest corotation radius that could be performed for this galaxy. This corotation radius $R_{\mathrm{CR}} = 3.15\,\mathrm{kpc}$, measuring about 3 exponential disk scale lengths in K', corresponds to a spiral pattern rotation of $\Omega_{\mathrm{p}} \approx 48\,\mathrm{km\,s^{-1}kpc^{-1}}$. This puts the corotation radius in the radial range that separates the inner disk with the stronger spiral and the outer disk with the flocculent morphology (see Figure 6.5). According to the discussion from Section 2.3, it is indeed found that at the corotation the number of star forming regions is reduced. Solely in the the inner arm emerging to the west shows few H II-regions at the corotation radius. This fact might be regarded as some evidence that even though, due to numerical limitations, no faster pattern speeds could be probed the location of the corotation resonance is probably well determined.

Certainly something is happening to the spiral pattern between the inner and the outer disk that makes it lose strength. However, since the model-to-observations comparison cannot be very detailed in the outer disk, there is no solution to the question if a single pattern rotation speed is a good approximation for NGC 3810.

6.1.3.2. The gas velocity field

The observed gas velocity field from NGC 3810 is governed by a large amount of small scale fluctuations and jumps. There are almost no measurements that exhibit a longer radial range of smooth, unshocked gas kinematics. Certainly, most of these small scale wiggles are not induced by gravity.

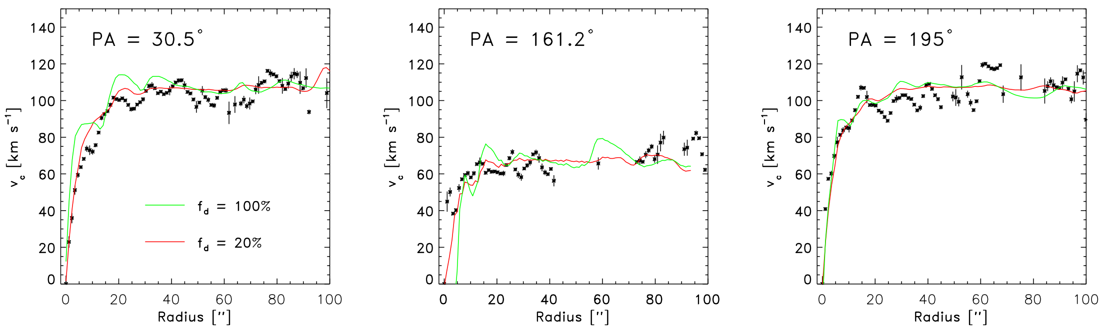

Figure 6.6 Example of the comparison of the simulation results to the observed kinematics of NGC 3810. The "maximal disk" and "minimal disk" velocity field are shown for three position angles. Presented are results from simulations assuming a fast pattern rotation $\Omega_p \approx 48\,\mathrm{km\,s^{-1}\,kpc^{-1}}$ ($R_{CR} = 3.15$ kpc). The full comparison is shown in Appendix A.

In Figure 6.6 the comparison of the simulations with the observed data is presented for a sample of three position angles of NGC 3810, illustrating the overall fit quality. Shown are the simulated curves for the maximal disk case ($f_d = 100\,\%$ in green) and the one for the setup using the most massive halo ($f_d = 20\,\%$ in red). An overview on all position angles is provided in the Appendix A. Like for NGC 4254, the global shape of the rotation curve gets very well approximated by the models. This applies to all five simulated disk-halo combinations, including the two shown extreme cases. On small scales the situation is clearly less satisfying. Although a few wiggles overlap fairly well, most of the structures cannot be reproduced by the simulated gas velocity fields. Especially in the outer parts of the disk, the agreement between simulated and observed wiggles is poor.

As for NGC 4254, the global least squares analysis loses much of its significance in such a case. By using the χ^2-analysis the least deviant model velocity field can be identified. This could in principle allow two conclusions: either the best matching case or the least disagreeing simulation result. If the majority of the kinematic structures do not match or coincide with the observations, the latter of the above will most likely be the preferred scenario from the χ^2-analysis. The left partition of Figure 6.7 gives an overview on the results from the global χ^2-analysis. Larger boxes indicate a smaller χ^2/N-value and thus a smaller deviation from the observed data. It must be noted, that – like for NGC 4254 –

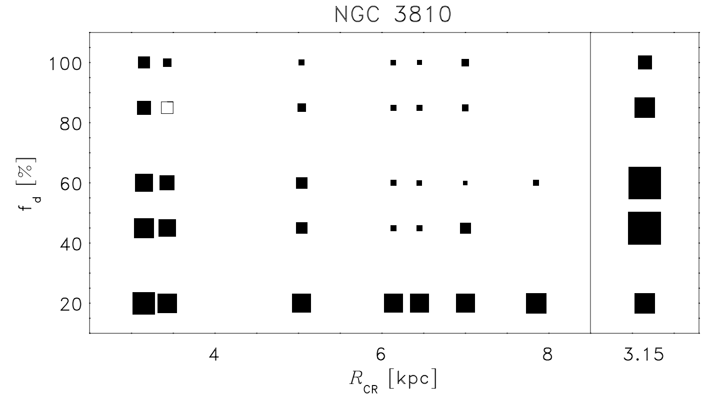

Figure 6.7 Graphical presentation of the global χ^2-analysis of all the velocity simulations for NGC 3810 (left partition). At right, the χ^2-analysis of the reduced data set is shown for a corotation radius $R_{\rm CR}$ = 3.15 kpc. Large boxes indicate better agreement between the simulated velocity field and the observed kinematics. The open box represents the simulation that terminated before passing the initialization phase. The actual χ^2-values can be found in Appendix A.

an additional systematic error of $9.5\,\mathrm{km\,s^{-1}}$ has been added to each observed data point (see Section 4.3.2).

The global χ^2-distribution across the parameter space for NGC 3810 appears very smooth. While for large disk mass fractions and large corotation radii the agreement between the simulations and the data is worst, it almost continuously turns better for lighter disks and smaller corotation radii. The trend in corotation reflects a real effect, since for the fast pattern rotation the morphology match of the gas density turned out best. However, the trend for the lighter disks to provide a better fit to the observed rotation curves is likely to be a systematic effect from the global χ^2-analysis. As discussed above, on small scales the simulations fail to reproduce the structure of the observed rotation curves in a sufficient way. In light of this, the models that exhibit the least non-axisymmetric structures from the two-dimensional simulations will be the ones that deviate the least from the observed rotation curves, to which the axisymmetric gravitational potential of the galaxy was tuned to fit.

However, following the method explained in Section 4.3.2.1, it can be seen that if considering only the parts of the observed velocity field where the gas dynamics appear to be dominated by gravitational forces, a medium disk solution is preferred (see the right partition of Figure 6.7). In this case the model with the lightest stellar disk turns out to give a less good agreement to the data as compared to the $f_d = 45$ and 60 % models. During the rejection process of non-gravitationally induced wiggles, 51 % of the data points were discarded from the comparison (see Appendix A for details). This implies that about half of the gas dynamic small scale structures could not be related to gravitational influence of the stellar spiral. Thus, NGC 3810 does certainly not qualify as an excellent laboratory for this study. Nevertheless, the results are in favor of a dynamically fairly important stellar disk, indicating that the mass comprised in stars roughly balances the mass of the dark halo inside the optical radius of the disk.

6.2. NGC 3893

NGC 3893 is a grand design Sc galaxy located in the Ursa Major Cluster of galaxies. The galaxy is interacting with the Magellanic dwarf type galaxy NGC 3896, located at a projected distance of $3\farcm9$ to the south-east. Radio data reveal a H I-bridge between NGC 3893 and NGC 3896 (Verheijen & Sancisi 2001). The most striking optical evidence for the interaction is a very clear two-arm morphology at all radii and the slightly disturbed symmetry, seen in the north-eastern arm of NGC 3893. The strong $m = 2$ spiral has an arm to inter-arm contrast of $0.4 - 0.5$ mag in K'. The interacting arm shows a kink and a change in the pitch angle at a position angle of 150° and another one at a position angle of 95°. Furthermore the interacting arm exhibits a over-abundance of H II-regions relative to the rest of the galaxy, indicating enhanced star formation. Despite of its disturbed morphology, the radial brightness profile is fairly well described by a double exponential model profile. Only beyond a radius of $\approx 100''$ the disk appears slightly brighter. The galaxy's K-band exponential disk scale length of $21\farcs9$ corresponds to 1.8 kpc, if a distance of 17 Mpc is assumed towards NGC 3893, taken as an average literature value. See also Figure 6.8 for an illustration of the radial K' profile.

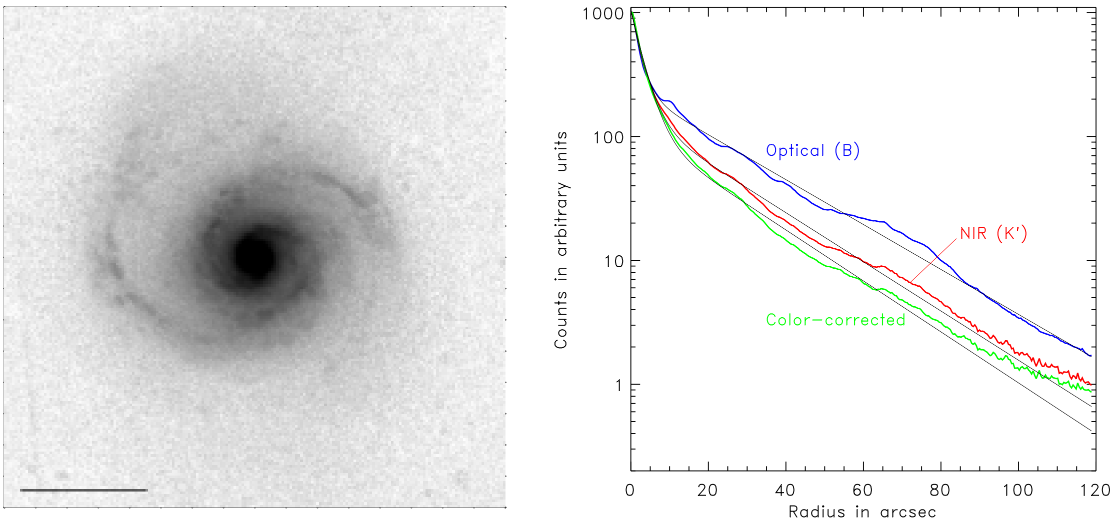

Figure 6.8 NGC 3893. At left the deprojected, color-corrected, H II-region cleaned image of NGC 3893 is shown. It was used as an input to calculate the gravitational potential of the stellar disk contribution to the total gravitational potential. The scaling bar is $1'$. At right, the effect of the color correction on the disk scale length of NGC 3893 is shown. The azimuthally averaged radial light profile is fairly well approximated by a double exponential disk model (black lines). The color correction causes the profile to steepen by only 3.5 %, as compared to the K-band.

NGC 3893 has a total blue magnitude of $B_T = 11.2$ mag and the disk measures about 4.3×2.5 arcminutes on the sky, although further out very faint arms can still be traced in long exposures. The major axis position angle, PA $= 166\fdg0$, and the inclination of the disk, $i = 42\fdg0$, were determined from the measured kinematics. The inclination corrected rotation curve rises gently and does not reach the flat part of the rotation curve inside

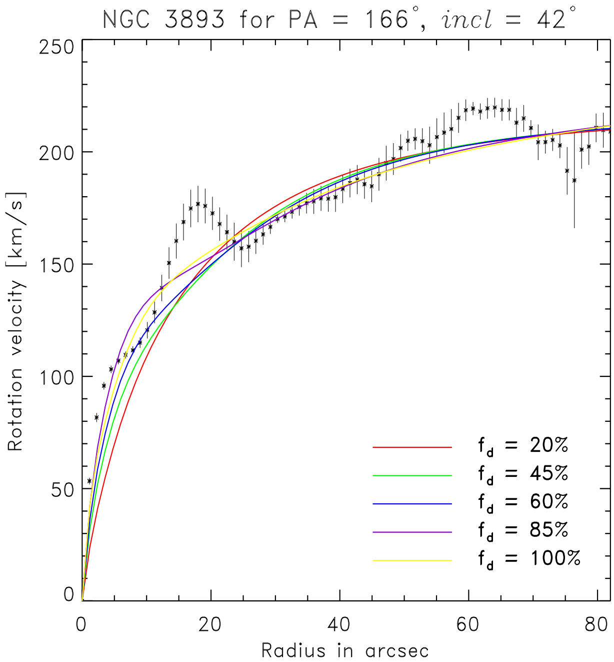

Halo parameters

f_d [%]	R_{core} [kpc]	v_∞ [$km\,s^{-1}$]
20	1.04	228
45	1.55	230
60	1.96	233
85	3.43	262
100	4.62	287

Figure 6.9 Rotation curve comparison for NGC 3893. The five axisymmetric model potentials for different fractions of the stellar disk potential yield rotation curves that are very similar, but differ slightly in steepness of the inner rising part.

a radius of 85″. At this radius the rotation velocity reaches about $220\,km\,s^{-1}$. From H I-observations it is known that further out the rotation curve drops to $\approx 150\,km\,s^{-1}$ (Verheijen & Sancisi 2001), most likely influenced by the interaction. From the K-band images, there is no evidence for a bar at the center. However, other authors find evidence for a weak bar in optical images (Eskridge et al. 2000).

The color correction has no drastic effect on the overall morphology of NGC 3893. While the clear $m = 2$ spiral structure remains very prominent, the largest effect of the of the correction is seen in the interacting arm. There the arm inter-arm contrast gets reduced to $\approx 80\,\%$ of its K-band value. This is certainly the result from a younger stellar population occupying the north-eastern arm, where the interaction acted as a trigger to induce recent star formation. For NGC 3893, the steepening of the radial profile due to the color correction amounts to only 3.5 % (see also Figure 6.8 and Table 4.2). This leads to the conclusion that the induced star formation yielding younger, and therefore bluer, stellar populations found in the interacting arm is a very local effect, i.e. local within the disk and in time. If the interaction had taken place on large timescales the younger stellar population would have spread across the disk, leading to a overall blue outer disk.

Five models of the total gravitational potential were also prepared for NGC 3893, varying the stellar disk mass fraction f_d. Figure 6.9 shows the rotation curves from the five model potentials, as compared to the observed kinematics. The Table accompanying Figure 6.9 lists the core radii and asymptotic rotation velocities of the five pseudo-isothermal halo models used to assemble the total galaxy potentials. All of the axisymmetric model rotation curves can approximate the galaxy's observed rotation curve fairly well. However, in the inner parts the models with a higher stellar disk contribution provide a better match to the observations. The 'bump' at 17″, which is caused by the strong spiral arms, cannot be reproduced by axisymmetric models. To achieve this, 2D hydro-simulations are needed.

Table 6.2 Hydrodynamic simulations for NGC 3893. Given is the duration of the individual simulation in units of 10^6 years.

f_d	corotation radius R_{CR} [kpc]							
[%]	3.18	5.47	6.46	7.06	7.55	8.56	9.84	∞
20	281*	1064	1064	1064	1064	1064	1064	1064
45	—	1064	1064	1064	1064	1064	1064	1064
60	281*	1064	1064	1064	1064	1064	983	1064
85	281*	1064	441*	1064	1064	963	1064	1064
100	281*	1064	1064	1064	1064	1064	1064	1064

* Note: This run terminated before ending the initialization phase of the simulation, which occurs at 550 Myrs.

6.2.1. Performing the hydrodynamical gas simulations

For modelling the two-dimensional gas surface densities and velocity fields for NGC 3893 again a Cartesian grid of 201×201 grid cells was chosen. The adopted distance towards NGC 3893 of 17 Mpc puts the grid cell size to 97.9 kpc. According to this cell size and a gas sound speed $c_s = 10\,\mathrm{km\,s^{-1}}$, the sound crossing time for one cell is about 13.8 Myrs, which puts the empirical time of 40 sound crossing times to initialize the final potential for the simulation to 550 Myrs.

To find the spiral pattern speed Ω_p, the following corotation radii R_CR were modelled: R_CR = 3.18, 5.47, 6.46, 7.06, 7.55, 8.56, 9.84 kpc and no pattern rotation. Table 6.2 provides an overview of the runs that were performed for NGC 3893.

6.2.2. Results from the hydrodynamical gas simulations

6.2.2.1. The gas density

The pure two-arm morphology of NGC 3893 turns out to provide a more elementary basis for the simulations as compared to flocculent, multi-arm galaxies. In the simulation for the best matching corotation radius (Figure 6.10), the gas density renders very accurately the shape of the underlying spiral morphology. The strongest gas shocks come to lie where the spiral arms are best defined and most of the star forming H II-regions are located. Even beyond the corotation, which is indicated by the red circle, the shocks are well in place. Like for NGC 3810, outside corotation the simulation develops a long and continuous shock in response of the outskirts of the interacting arm. In the galaxy's inter-arm regions there are also some weaker shocks.

Given the good agreement of the gas density distribution with the galaxy's morphology, the pattern rotation of NGC 3893 can get determined very well. The best matching model places the corotation at the vicinity of about 3 exponential K' disk scale lengths, $R_\mathrm{CR} = 5.5 \pm 0.5\,\mathrm{kpc}$, corresponding to a pattern speed $\Omega_\mathrm{p} \approx 38\,\mathrm{km\,s^{-1}kpc^{-1}}$. On the other hand, a global pattern rotation speed might not hold for the interacting part of the spiral. As seen from Figure 6.10, beyond the corotation radius, the interacting spiral arm broadenes considerably. this indicates the disintegration of the density wave. Still, in the inner part, where the spiral exhibits a very symmetric pattern, the approximation with a single pattern rotation speed appears to work very well. The analysis of the kinematic data will eventually confirm this notion.

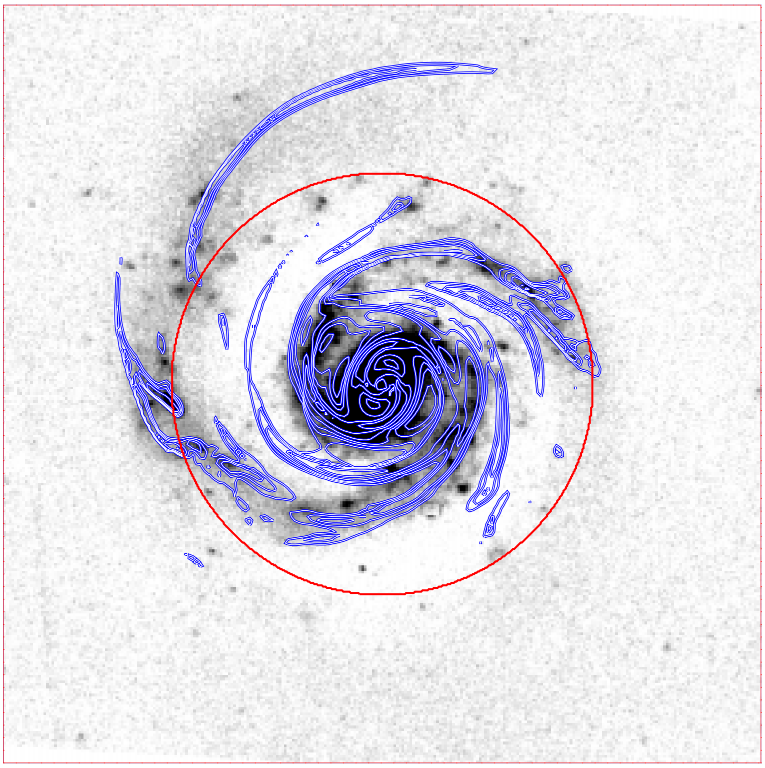

Figure 6.10 Simulation results of the gas density distribution overlaid in contours onto the deprojected K'-band image of NGC 3893. From the image an axisymmetric radial brightness profile has been subtracted to enhance the contrast of the spiral arms. The Figure shows the contours for the simulation with $\mathrm{f_d} = 100\,\%$ and a corotation radius (red circle) of 5.47 kpc. The full set of simulation results is shown in Appendix B.

6.2.2.2. The gas velocity field

Differing from NGC 3810 and NGC 4254, in the observed gas velocity field from NGC 3893 small scale wiggles and jumps are less prominent. As seen in Figure 3.2, the rotation curves along many slit positions are smooth and steady, revealing broad wiggles where the slit was crossing a spiral arm. The interpretation of this finding would be that the gas velocity field of NGC 3893 seems indeed to be governed by large scale gravitational effects rather than local gas bubbles and turbulences. These are favorable conditions for carrying out the hydrodynamic simulations.

In Figure 6.11 the comparison of the simulations with the observed data is presented for a sample of three position angles of NGC 3893, illustrating the overall fit quality. Shown are the simulated curves for the maximal disk case ($\mathrm{f_d} = 100\,\%$ in green) and the one for the setup using the most massive halo ($\mathrm{f_d} = 20\,\%$ in red). An overview on all position angles is provided in the Appendix B. The match of the $\mathrm{f_d} = 100\,\%$ simulation is striking! In the inner parts the wiggles found in the simulated velocity fields coincide almost perfectly with the observations. This applies also to most of the slit position angles that are not shown here, although in some cases the amplitude of the wiggles deviates slightly. This finding complements very well the good match of the gas density morphology with the underlying galaxy structure. At the outer parts of the rotation curves the agreement be-

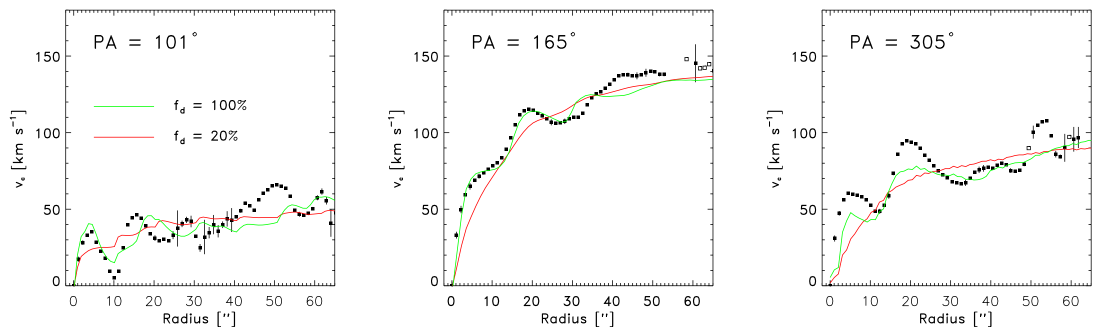

Figure 6.11 Example of the comparison of the simulation results to the observed kinematics of NGC 3893. The "maximal disk" and "minimal disk" velocity field are shown for three position angles. Presented are results from simulations assuming a pattern rotation $\Omega_\mathrm{p} \approx 38\,\mathrm{km\,s^{-1}\,kpc^{-1}}$ ($R_\mathrm{CR} = 5.47\,\mathrm{kpc}$). Clearly the maximum disk simulation provides an excellent fit to the observations. The full comparison is shown in Appendix B.

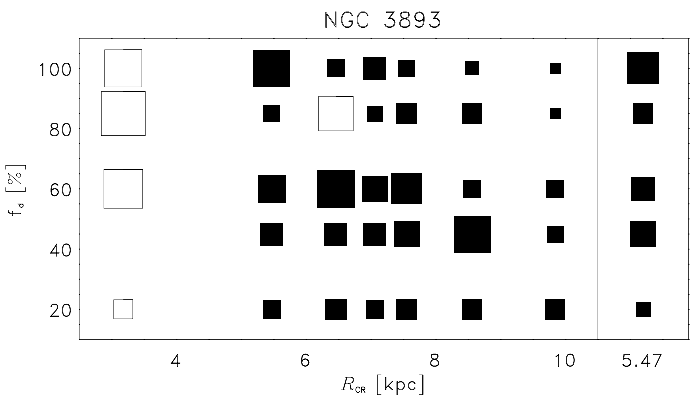

Figure 6.12 Graphical presentation of the global χ^2-analysis of all the velocity simulations for NGC 3893 (left partition). At right, the χ^2-analysis of the reduced data set is shown for a corotation radius $R_\mathrm{CR} = 5.47\,\mathrm{kpc}$. Large boxes indicate better agreement between the simulated velocity field and the observed kinematics. The open boxes represent simulations that terminated before passing the initialization phase. The actual χ^2-values can be found in Appendix B.

tween simulations and observations turns into a good global fit. Beyond $\approx 45''$ the wiggles in the observed velocity fields tend to exhibit a larger amplitude than what can be found in the simulations. Corotation is at $65''$.

Given the excellent overlap of features, the conditions are such that the global χ^2-analysis may yield conclusions about the mass composition within the galaxy. The left partition of Figure 6.12 provides an overview on the results from the global χ^2-analysis. Larger boxes indicate a smaller χ^2/N-value and thus a smaller deviation from the observed data. The best matching simulation results lie in the fast pattern rotation and high disk mass range. The open boxes denote simulations that terminated before passing the initialization phase. As discussed in Section 6.1.2, these runs tend to render a better fit than what the equilibrium state would yield. Still these simulations demonstrate that in the vicinity of the best fitting run ($R_{\mathrm{CR}} = 5.5\,\mathrm{kpc}; \mathrm{f_d} = 100\,\%$) the overall fit quality is generally high. The region of good agreement for the medium disk models is lacking the detailed fit quality on a wiggle-by-wiggle basis, that is found for the maximal disk simulation which is displayed in Figure 6.11.

The analysis of only the fraction of the velocity field, for which most likely gravity is the dominant driving force of the gas (see Section 4.3.2.1 for a description of the method) provides even stronger support to this trend. See the right partition of Figure 6.12. Eventually, the least squares comparison is not very sensitive to non-gravitationally induced gas dynamic features. The selection process rejected about 40 % of the data points from the observations (see Appendix B for a Figure), with almost no effect on the conclusions. Thus, the analysis of NGC 3893 yields a very robust result and it can be concluded that a maximum disk is needed to explain the observations well.

Eventually, a detailed look at the data reveals that the good agreement between observations and simulations mainly relies on the inner part of the disk. In the outer parts the simulations fail to predict the disk kinematics as detailed, pointing to dynamic processes, most likely correlated with the interaction, that cannot get treated with a single spiral pattern speed.

6.3. NGC 5676

NGC 5676 is a Sc starburst galaxy located in a small group of galaxies with 11 reported members (Garcia 1993). It reveals a fairly strong two arm grand design morphology. However, as it can be seen in the left panel of Figure 6.13, the deprojected spiral pattern shows frequent kinks making the inner spirals appear hexagonal. At a radius of about 30″ the spirals become smoother. While the eastern (left) arm continues for another 180° after the last kink, the western arm (right) breaks up and fragments into a more flocculent morphology. From the K-band images, there is evidence for a weak bar at the center. It is displayed in the right panel of Figure 6.13. Its position angle is at about 38° and its radius is about 12″, or 1.9 kpc.

Although situated in a group, no evidence for ongoing interaction has been reported. On the other hand, past interactions certainly occured and might have triggered the spiral density wave and the starburst. The radial brightness profile is very well described by a double exponential model profile (see Figure 4.1a). The galaxy's K-band exponential disk scale length of 22.″4 corresponds to 3.6 kpc, if a distance of 33 Mpc is assumed towards NGC 5676, taken as an average literature value. NGC 5676 has a total blue magnitude of $B_T = 11.9$ mag and the disk measures about 3.9×1.9 arcminutes on the sky at the 22 K-mag per square arcsecond isophote. The major axis position angle, PA = 45.°8, and the disk inclination, $i = 64.°0$, were determined from the measured kinematics.

The inclination corrected rotation curve rises very steeply at the center and reaches the flat part of the rotation curve at a radius of 25″ (see Figure 6.14). The rotation velocity levels at about 240 km s^{-1}, which is the highest rotation velocity of all galaxies from the sample with measured kinematics.

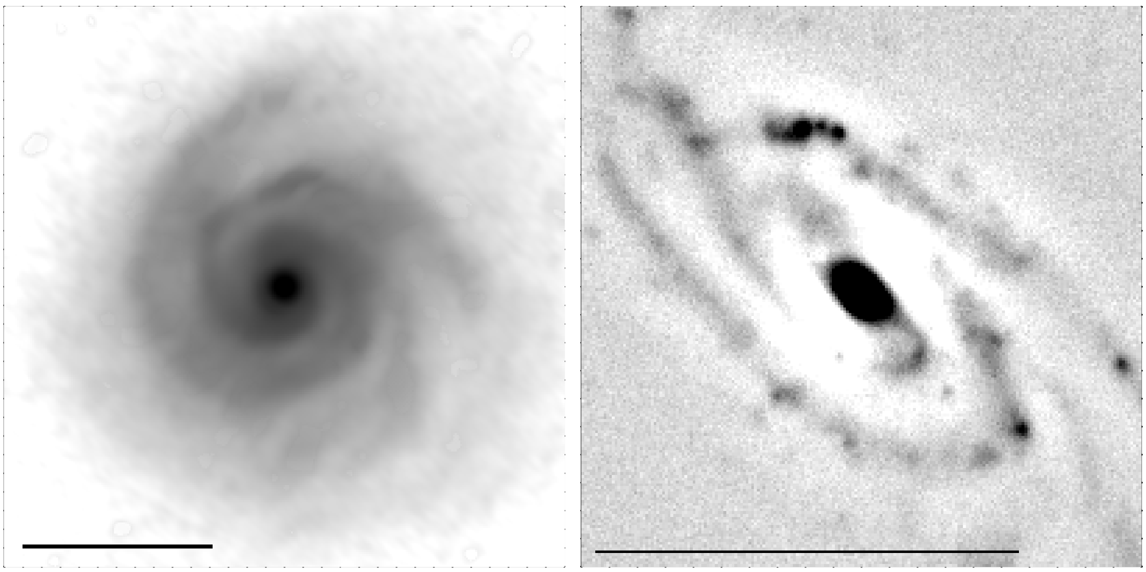

Figure 6.13 NGC 5676. At left the deprojected, color-corrected, H II-region cleaned image of NGC 5676 is shown. It was used as an input to calculate the gravitational potential of the stellar disk contribution to the total gravitational potential. At right, the central region of NGC 5676 (K-band) is shown. Using the unsharp masking technique, a weak central bar can be identified. The horizontal bar at the bottom of both images measures 1′.

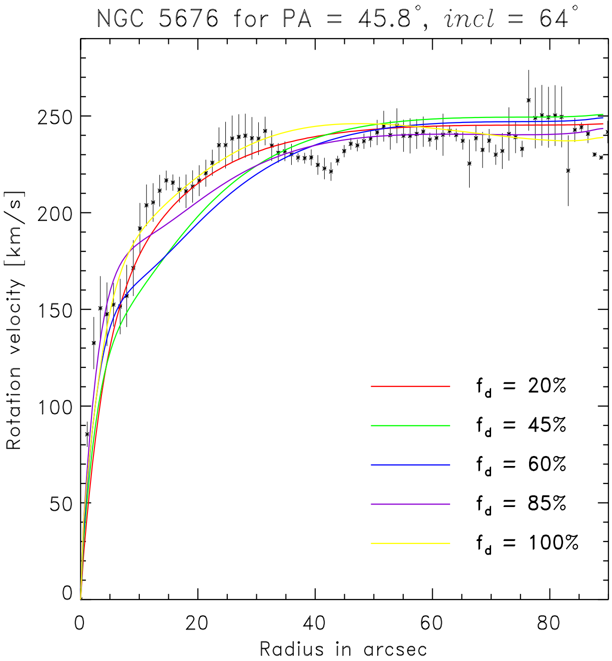

Halo parameters

f_d [%]	R_{core} [kpc]	v_∞ [km s^{-1}]
20	0.82	240
45	2.09	240
60	3.30	240
85	8.87	280
100	12.0	280

Figure 6.14 Rotation curve comparison for NGC 5676. The five axisymmetric model potentials for different fractions of the stellar disk potential yield rotation curves that fit fairly well with the observed rotation curve. However, the steep central rise from 10″ to 30″ is approximated best by either the maximal or minimal disk model.

The color correction clearly enhances the $m = 2$ spiral structure of NGC 5676. Some of the features in the disk appear very blue and hence get largely reduced in the color corrected image (for example the inter-arm feature seen in the upper left corner of the K-band image, displayed in the right panel of Figure 6.13). However, NGC 5676 might have a considerable amount of dust in the disk, that obscures especially at optical wavelengths. Since the optical image has only a moderate resolution of 2.″3 (FWHM) it is very hard to tell from the image, if a region is less bright because of dust or because less star formation activity. High amounts of dust can in principle cause the color correction to fail at places where the dust is optically thick. On the other hand, the color correction works well in the presence of dust as long as not all the light gets absorbed. Moreover, in galaxies with violent star formation going on – like NGC 5676 – the population differences are large and the color correction is expected to have a stronger effect on the two dimensional mass distribution. However, the IMF of starburst galaxies is distincly different from the universal IMF that was used to derive the M/L to color relation. This fact leads to the conclusion that even the color corrected K-band image still does not provide a highly accurate mass map of the galaxy. In light of this, even if the mass map will not be perfect, applying the color correction still yields a better mass map than just the K-band image and that it is worthwhile doing it. The color correction causes the arms to appear more continuous and better defined. The radial K-band light profile steepens by 12.9 % as a result from the color correction, still remaining exponential.

NGC 5676's inclination on the sky (64°) is rather high and the deprojected image has been convolved with a transposed distortion function, as shown in Figure 4.3. Additionally, even though the center reveals the weak bar, the very center was replaced by a truly axisymmetric model of the inner part. This was done to avoid problems at the very center, when running the hydrosimulations. Due to the high rotation velocity and the steep cen-

Table 6.3 Hydrodynamic simulations for NGC 5676. Given is the duration of the individual simulation in units of 10^6 years. The dynamical time scale for NGC 5676 is 383 Myrs.

f_d	corotation radius R_{CR} [kpc]										
[%]	5.6	6.6	7.65	8.6	9.6	10.6	11.6	12.6	13.6	14.16	∞
20	—	—	902	902	902	902	902	902	902	—	—
45	571	1052	1292	1292	1292	1292	1292	691	781	812	1292
60	—	—	602*†	452*†	572*†	—	873	993	873	843	1714
85	—	—	511*	571	541	511*	511*	511*	541	—	—
100	—	—	541	511*	511*	511*	541	451*	451*	511*	—

Notes: * This run terminated before ending the initialization phase of the simulation, which occurs at 529 Myrs.
† The f_d = 60 % simulations were performed on a grid with a larger cell size, leading to longer initialization phases (704 Myrs).

tral velocity gradient, NGC 5676 is very susceptible to creating these extremely rarefied gas conditions in the simulations that were described in Section 6.1.2.

Also for NGC 5676 five models of the total gravitational potential were prepared, varying the stellar disk mass fraction f_d. Figure 6.14 shows the rotation curves from the five model potentials, as compared to the observed kinematics. The Table accompanying Figure 6.14 lists the core radii and asymptotic rotation velocities of the five pseudo-isothermal halo models used to assemble the total galaxy potentials. The model rotation curves match fairly well with the observed rotation curve, however not as well as it can be achieved for other galaxies in the sample. A reason for this is the steep rise in the center and the righ rotation velocity. For the "medium-disk" models the isothermal sphere with a core is not flexible enough to account for the steep rise, lacking massive contribution from the small bulge and the inner disk. As it will be seen later, the two dimensional gas simulations yield velocity fields that reproduce the observed rotation curves better than the axisymmetric model rotation curves.

6.3.1. Performing the hydrodynamical gas simulations

The two-dimensional gas modelling for NGC 5676 was performed on a 301×301 Cartesian grid. The larger grid size was motivated by the fact the NGC 5676 is located at a distance of 33 Mpc, thus relatively far away. The grid was scaled to yield a similar cell size in real dimensions within the galaxy. In this setup the length of one grid cell measures 95.1 pc. According to this cell size and a gas sound speed $c_s = 10\,\mathrm{km\,s^{-1}}$, the sound crossing time for one cell is about 13.2 Myrs, which puts the empirical time of 40 sound crossing times to initialize the final potential for the simulation to 530 Myrs. Only for the earliest runs (f_d = 60 %), the grid cell size was larger (127 pc), putting the initialization time for the code to 704 Myrs. The later increase in grid resolution was motivated by the gain of higher accuracy as well as reducing the simulation time fur the runs.

To find the spiral pattern speed Ω_p models with the following corotation radii R_{CR} were simulated: R_{CR} = 5.6, 6.6, 7.65, 8.6, 9.6, 10.6, 11.6, 12.6, 13.6, 14.16 kpc and no pattern rotation. Table 6.3 provides an overview of the runs that were performed for NGC 5676.

As seen from Table 6.3, the premature termination of simulations is a serious issue for NGC 5676. For heavy disk simulations, all the runs terminated close to the end of the initialization phase. The main reason for this to happen, is the very steep velocity gradient of $\approx 400\,\mathrm{km\,s^{-1}}$ within a radial scale of $\approx 40''$ at the center. Furthermore the small bar introduces additional non-axisymmetric structures, that cause strong shocks in the simulated gas flow. As a preventive strategy, the center of the mass map, which was used as the input to calculate the stellar disk contribution of the gravitational potential, was replaced by a truly axisymmetric model in order to minimize the non-axisymmetric central structures in the final potential. Even though, for heavy disks, the runs encounter extreme shocks at the center that eventually produce negative gas densities at certain grid cells. In a second attempt, simulations were done using a higher gas sound speed of $c_s = 15\,\mathrm{km\,s^{-1}}$, intending the gas to respond less to non-axisymmetric features in the potential. Also this modification could not extend the run time of the simulation considerably. These results are not discussed.

Yet, the simulation situation for NGC 5676 is very unsatisfactory. As seen in the following section, preliminary conclusions can be drawn, but a thoroughly successful modelling of the galaxy still needs to be achieved. At the present status of the simulation process there is still a variety of hitherto unexplored options that offer good chances for success. So far it seems that the very bright emission of the many strong star forming regions in the arms of this starburst galaxy has not been corrected well enough by the standard treatment that was described in Chapter 4.

6.3.2. Preliminary results from the hydrodynamic gas simulations

6.3.2.1. The gas density

The spiral structure of NGC 5676 is fairly regular, but still the arms deviate from smooth logarithmic radial profiles. Apparently this behavior is challenging for the simulations to match. Figure 6.15 shows the gas density distributions resulting from two simulations which yield the best matching morphology. The gas density contours are overlaid onto the deprojected K-band image, treated by the unsharp masking technique to enhance the contrast of the underlying spiral structure. While the simulation with the slower pattern speed ($\Omega_\mathrm{p} \approx 21\,\mathrm{km\,s^{-1}kpc^{-1}}$ or $R_\mathrm{CR} = 11.6\,\mathrm{kpc}$, right panel of Figure 6.15) reproduces very well the inner spiral structure, the one with the faster pattern speed ($\Omega_\mathrm{p} \approx 25\,\mathrm{km\,s^{-1}kpc^{-1}}$ or $R_\mathrm{CR} = 9.6\,\mathrm{kpc}$, left panel of Figure 6.15) yields a better fit to the outer spiral. In both simulations the modelled gas shocks follow rather closely the spiral structure of the arm emerging from the north top of the bar for about 270°. Further out, other shocks, coming from the inner or outer inter-arm region then take the place of the primary shock. The replaced shock quickly loses its strength and fades away. Thus, the simulated gas shocks come to lie in the vicinity of nearly all arm parts and fragments.

The fact that simulations for different pattern speeds tend to reproduce the spiral structure better at different radii can be regarded as evidence that the pattern speed is not constant for the entire disk. Additionally, if the velocity field is considered, it can be found that there is a severe mismatch at the central arcseconds too, which indicates that also the dynamic processes at the bar cannot be modelled successfully along with the rest of the disk. In light of this, describing the disk dynamics of NGC 5676 by a single pattern speed

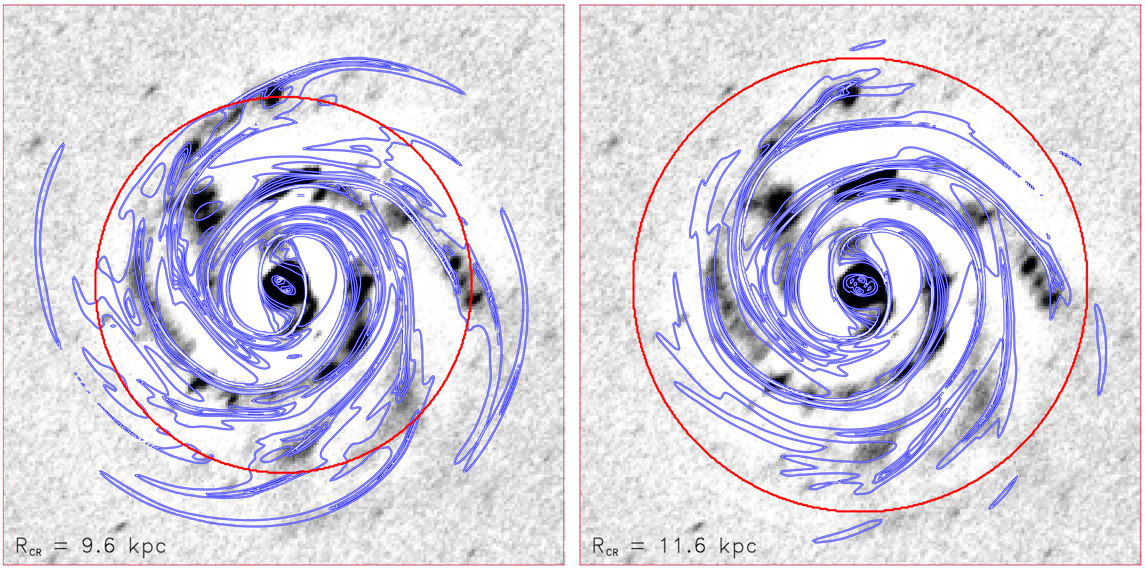

Figure 6.15 Simulation results of the gas density distribution overlaid in contours onto the deprojected K'-band image of NGC 5676. From the galaxy image a unsharp mask was subtracted to enhance the contrast of the spiral arms. The Figures show the contours for the simulation with $f_d = 85\,\%$ and corotation radii (red circles) of 9.6 and 11.6 kpc. The full set of simulation results is shown in Appendix D.

might not be appropriate. However, the range of best fitting pattern speeds is still rather narrow ($R_{CR} \approx 9 - 12\,$kpc). Furthermore, as it will be seen from the velocity comparison, the simulations with $R_{CR} = 11.6\,$kpc render very well the observed gas dynamics across most of the disk.

Thus, a good matching corotation model places the resonance at the vicinity of about 3 exponential K' disk scale lengths, $R_{CR} = 11^{+1}_{-2}\,$kpc, corresponding to a pattern speed $\Omega_p \approx 22\,\mathrm{km\,s^{-1}kpc^{-1}}$. In this case the corotation resonance is located in the direct vicinity to where the stellar spiral ends. Beyond corotation there is no regular spiral structure.

6.3.2.2. The gas velocity field

The observed gas velocity field of NGC 5676 is governed by a very steep rise at the center, levelling at $\approx 240\,\mathrm{km\,s^{-1}}$ along the major axis position angle at about 45° (see Figure 6.16). In general, the gas velocity field reveals a considerable amount of small scale structure. Scaling with the overall high rotation velocity there are many observed abrupt velocity jumps in the range of 30 – 50 $\mathrm{km\,s^{-1}}$. The observed data comprise only 7 slit positions, missing one measurement at the 0° position angle.

In Figure 6.16 the comparison of the simulations with the observed data is presented for a sample of three position angles of NGC 5676, illustrating the overall fit quality. Shown are the simulated curves for the near maximal disk case ($f_d = 85\,\%$ in green) and the one for the setup using the most massive halo ($f_d = 20\,\%$ in red). The match of the $f_d = 85\,\%$ simulation is very good along the displayed postion angles. Even some of the small scale wiggles are reproduced very accurately. As it is appearent from the overview on all position angles in Appendix D, for most position angles the comparison turns out

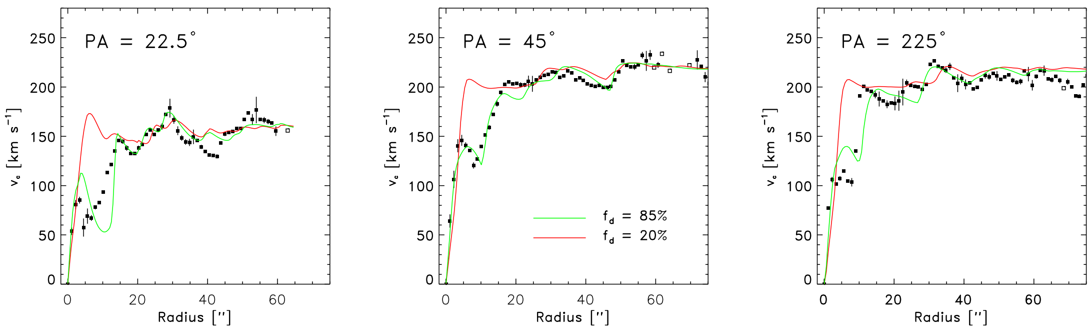

Figure 6.16 Example of the comparison of the simulation results to the observed kinematics of NGC 5676. Velocity field are shown for three position angles. Presented are results from simulations with $f_d = 20$ and 85 %, assuming a pattern rotation $\Omega_p \approx 21\,\mathrm{km\,s^{-1}\,kpc^{-1}}$ ($R_{CR} = 11.6$ kpc). There are severe discrepancies in the central parts. The full comparison is shown in Appendix D.

very good. Only in the inner $\approx 20''$ the simulated velocity fields exhibit exceedingly high velocity jumps, that eventually grow to such magnitudes that the simulation terminates prematurely. These extreme shocks are associated with the steep velocity gradient in the central velocity field of NGC 5676 and the presence of a small bar in the same region. This central bar could further possess a pattern speed, differing from that of the disk, introducing even more dynamic challenges for the simulations. In light of this, it must be pointed out that the $f_d = 85\,\%$ results, which are displayed in Figure 6.16, are indeed from a run that did not reach the final, stationary simulation phase. The run crashed at the timestep where the final realistic, non-axisymmetric gravitational potential was being turned on. The $f_d = 20\,\%$ simulation proceeded for more than a galactic dynamical time scale beyond this point. In fact, as seen from the results from the full χ^2-analysis that is presented in Figure 6.17, none of the heavy disk simulations proceeded significantly past the initialization phase.

Nonetheless, there is reason to argue that the $f_d = 85\,\%$ scenario is characteristic to the galaxy, and not just a numerical effect. First, the wiggle-to-wiggle agreement between the simulations and observations is undoubtedly better for the heavy disk model. Second, as seen from Figure 6.18, the evolution of the fit quality during the initialization phase of the simulation proceeds towards even better agreement (smaller χ^2) until the run terminated. It seems safe to extrapolate that median(χ^2) lies in the close vicinity of the last fit even beyond simulation timestep 18, after which the stationary simulation conditions are accomplished. The better fit quality of the $f_d = 20\,\%$ models as compared to the 45 and 60 % models is a result from the smoother and more axisymmetric model rotation curve. The basic axisymmetric disk model was tuned to match the overall rotation curve. This effect has been discussed for NGC 3810.

As a conclusion of this discussion, it seems fair to state that the simulations provide evidence for a heavy disk scenario in NGC 5676, even though the simulations did not yet provide an entirely satisfactory degree of completeness. A disk mass fraction $f_d \approx 85\,\%$ indicates that about 2/3 of the total mass inside 2.2 K-band disk scale lengths is contributed from the stellar disk. The core radius of the pseudo-isothermal halo is in that case in the range of several disk scale lengths. In this scenario, the halo begins only beyond the extent of the bright stellar disk to dominate the dynamics of the galaxy.

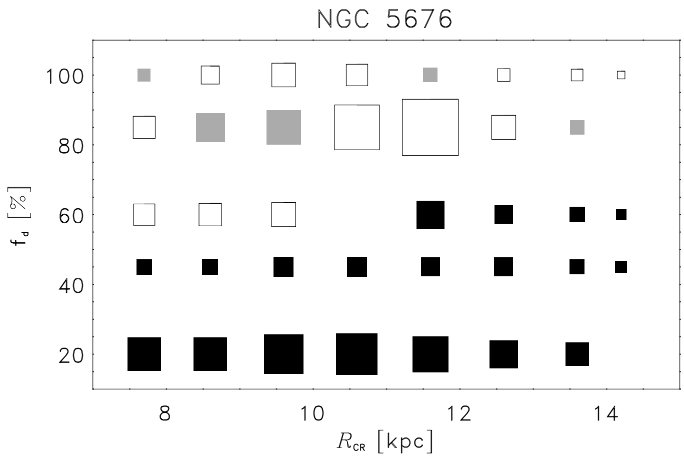

Figure 6.17 Graphical presentation of the preliminary, global χ^2-analysis of all the velocity simulations for NGC 5676. Large boxes indicate better agreement between the simulated velocity field and the observed kinematics. The open boxes represent simulations that terminated before passing the initialization phase. Grey boxes represent simulations that terminated immediately after reaching the stationary simulation phase. Premature terminations are a serious issue for NGC 5676.

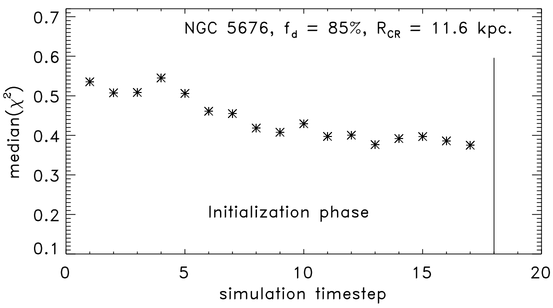

Figure 6.18 Evolution of the fit quality of the $f_d = 85\,\%$, $R_{CR} = 11.6$ kpc simulation during its initialization phase as measured from the median(χ^2) from the comparison. The simulation terminated during the calculation of timestep 18. The simulation evolves towards a better fit quality and might be safely extrapolated into the stationary simulation phase.

6.4. NGC 6643

NGC 6643 is probably the least suited galaxy for this experiment that is in the sample. Although it is classified as Sc, the galaxy reveals a very flocculent morphology with many star forming regions and knotty arms. In the NIR, the spiral structure is more pronounced, however, the arms appear still knotty and the arm to inter-arm contrast is very variable: 0.2 – 0.6 K'-mag. The regular two-arm spiral that direcly emerges from the tiny bulge breaks up into several arm pieces at a radius of about $20''$. These arms continue to wind outward for $\approx 180°$ with changing pitch angles. At the radius where the spiral breaks its symmetry, there is a massive over-abundance of star forming H II-regions. This over-abundance is also distincly notable in the radial brightness profiles, shown in the right panel of Figure 6.19. At the radial range from about 15 to $25''$ the brightness in B increases while in K' it stays constant. The color corrected radial profile almost entirely corrects this discontinuity and produces a very smooth exponential profile. This can be considered as a strong argument in favor of the color correction method. Especially, since for NGC 6643 it is not obvious that the color correction should work accurately. Like NGC 3810, also NGC 6643 was studied by Elmegreen et al. (1999) looking for underlying NIR symmetric structures in optically flocculent galaxies. These authors argued that dust might play a major role in explaining the flocculent optical appearance. Also Evans (1993) finds high dust extinction in the central region of NGC 6643. As discussed already for the case of NGC 5676, strong dust extinction might corrupt the outcome of the color correction. However, considering the above, the color correction seems to yield a much better mass map than the K-band image would be.

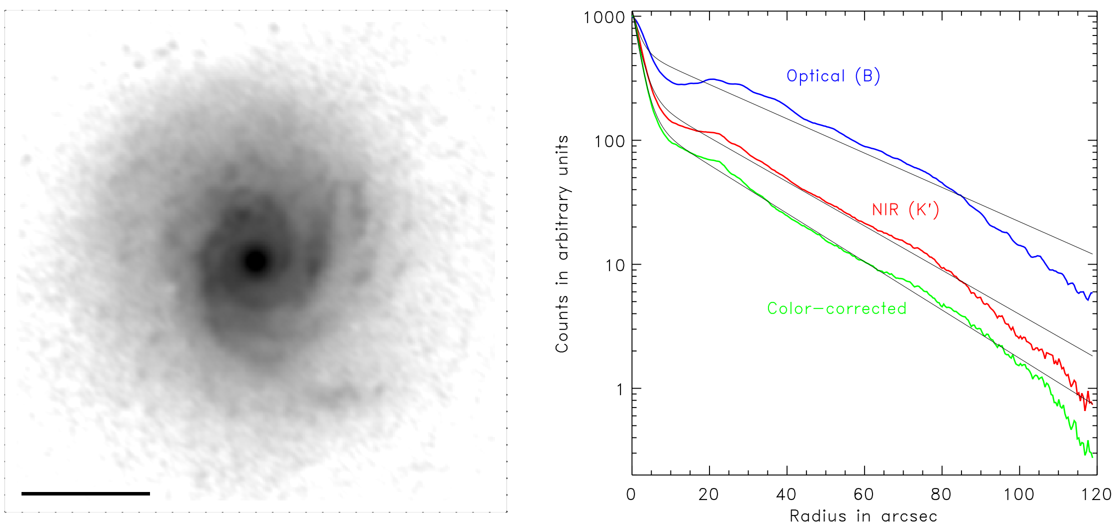

Figure 6.19 NGC 6643. At left the deprojected, color-corrected, H II-region cleaned image of NGC 6643 is shown. It was used as an input to calculate the gravitational potential of the stellar disk contribution to the total gravitational potential. The bar is $1'$. At right, the effect of the color correction on the disk scale length of NGC 6643 is shown. Note the deviation of the optical and K-band azimuthally averaged light profiles from a simple exponential. The model fit (black lines) of the color corrected profile steepens by 8.6 %, as compared to the K-band.

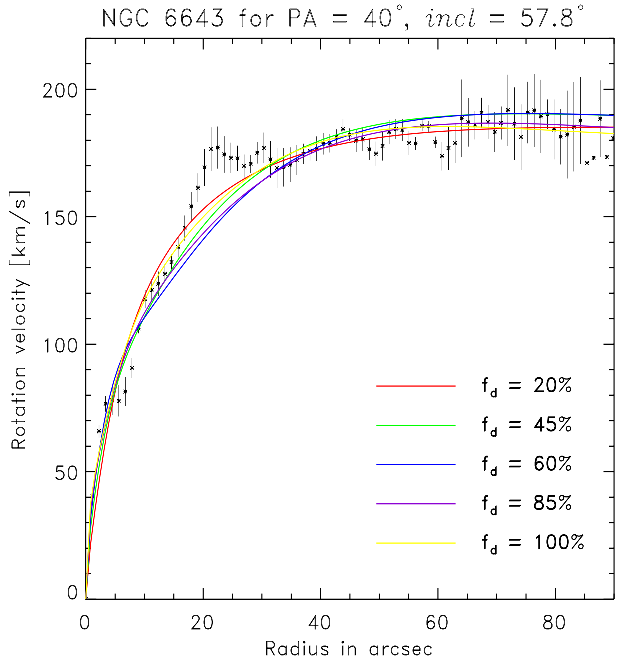

Halo parameters

f_d [%]	R_{core} [kpc]	v_∞ [km s^{-1}]
20	0.80	183.5
45	1.46	180
60	2.34	180
85	4.90	180
100	11.5	242

Figure 6.20 Rotation curve comparison for NGC 6643. The five axisymmetric model potentials for different fractions of the stellar disk potential yield rotation curves that are very similar and match well with the observed kinematics.

A distance of 23 Mpc was assumed towards NGC 6643, taken as an average literature value. At this distance the galaxy's K-band exponential scale length of $24''.4$ corresponds to 2.72 kpc. NGC 6643 has a total blue magnitude of $B_T = 11.8$ mag and the disk measures about 3.6×2.1 arcminutes on the sky at the 22 K-mag per square arcsecond isophote. The major axis position angle, PA $= 40^\circ.0$, and the inclination of the disk, $i = 57^\circ.8$, were determined from the measured kinematics. The inclination corrected rotation curve rises about linearly out to a radius of about $20''$, where there is a sharp break and the rotation curve levels to a constant value of $\approx 185\,\mathrm{km\,s^{-1}}$.

Five models of the total gravitational potential were prepared for NGC 6643, varying the stellar disk mass fraction f_d. Figure 6.20 shows the rotation curves from the five model potentials, as compared to the observed kinematics. All model rotation curves can explain the galaxy's observed rotation curve similarly well. Again, small scale features in the rotation curve like the "bump" at $\approx 20''$ cannot be matched by a simple axisymmetric model. The Table accompanying Figure 6.20 lists the core radii and asymptotic rotation velocities of the five pseudo-isothermal halo models used to assemble the total galaxy potentials.

6.4.1. Performing the hydrodynamical gas simulations

The two-dimensional gas modelling for NGC 6643 was performed on a 257×257 Cartesian grid. The grid size was chosen to yield a cell size in real dimensions within the galaxy that is similar to the others from the sample. In this setup the length of one grid cell measures 88.3 pc. According to this cell size and a gas sound speed $c_s = 10\,\mathrm{km\,s^{-1}}$, the sound crossing time for one cell is about 12.2 Myrs, which puts the empirical time of 40 sound crossing times to initialize the final potential for the simulation to 488 Myrs.

Table 6.4 Hydrodynamic simulations for NGC 6643. Given is the duration of the individual simulation in units of 10^6 years. The full potential is turned on at 488 Myrs.

f_d	corotation radius R_{CR} [kpc]							
[%]	4.18	5.1	6.0	6.5	7.00	8.0	9.0	10.0
20	782	842	842	842	842	842	842	842
45	842	842	842	842	842	842	842	842
60	692	842	842	—	842	842	842	842
85	842	842	842	842	782	511	842	842
100	661	782	601	812	—	842	842	842

To find the spiral pattern speed Ω_p, or equivalently the corotation radius R_{CR}, the following cases were modelled: $R_{CR} = 4.18$, 5.1, 6.0, 6.5, 7.0, 8.0, 9.0 and 10.0 kpc. Table 6.4 provides an overview of the runs, performed for NGC 6643. All runs carried on well beyond the initialization phase, so that premature simulation terminations are no issue for NGC 6643.

6.4.2. Results from the hydrodynamical gas simulations

6.4.2.1. The gas density

As mentioned before, the morphologic appearance of NGC 6643 does not qualify it as the perfect laboratory for the anticipated analysis. It does not exhibit a clear grand design spiral structure that helped to yield the good results for NGC 3893, but rather a patchy and flocculent morphology. Figure 6.21 shows the gas density distribution that resulted from two simulations with different corotation radii, which reproduce the galaxy's spiral structure comparably well. The gas density contours are overlaid onto the deprojected, unsharp masked K-band image, representing the underlying spiral structure. Since NGC 6643's arms do not wind with a constant pitch angle, the simulations encounter difficulties to reproduce all spiral features. While for the model with the faster pattern speed ($R_{CR} = 6.5$ kpc) the most prominent eastern (left) arm cannot be traced by one single gas shock, it still exhibits gas shocks in the vicinity of all major star forming regions. The scenario with the slower pattern speed ($R_{CR} = 8.0$ kpc) results in a fairly well overall matching morphology, only the arms in the gas simulation seem to wind too long, ultimately deviating from the observed morphology. Eventually, the spiral structure that develops in both gas simulations matches well with the galaxy's true spiral pattern. However, the results from the kinematic comparison favor the faster pattern speed model.

From the modelling, the location of the corotation resonance can be placed close to the end of the stronger spiral pattern. This is in the vicinity of about 2.4 exponential K' disk scale lengths, $R_{CR} = 6.5^{+1.5}_{-0.5}$ kpc, corresponding to a pattern speed $\Omega_p \approx 28.5\,\mathrm{km\,s^{-1}kpc^{-1}}$. Due to the moderate morphological match, the precision, with which the corotation can be determined is comparably low. However, the results from simulations outside the corotation range of $R_{CR} = 6 - 8$ kpc yield to even less satisfying comparisons (see Appendix E).

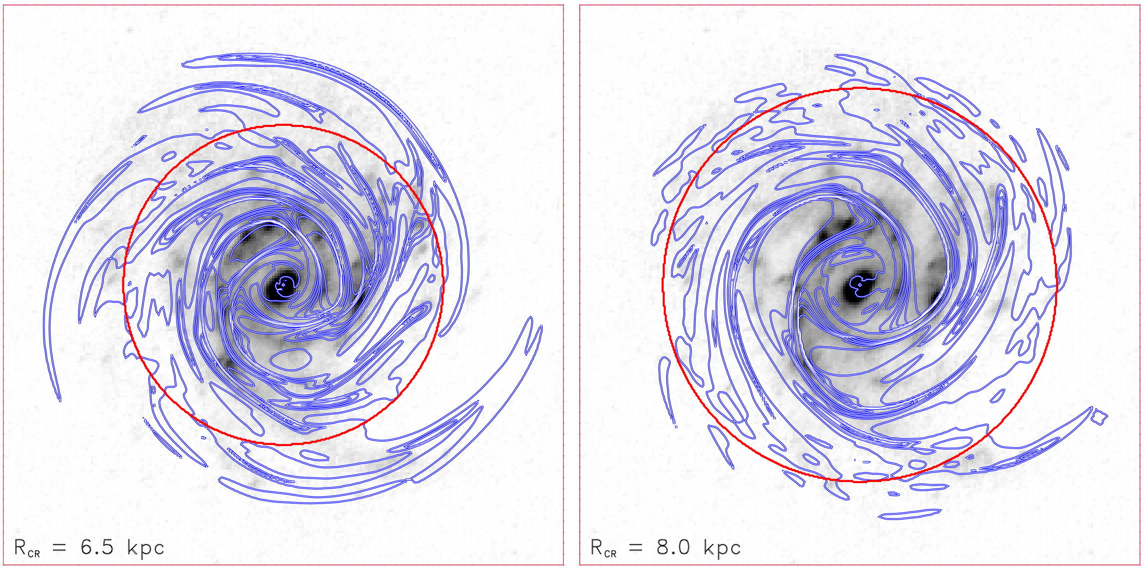

Figure 6.21 Simulation results of the gas density distribution overlaid in contours onto the deprojected K'-band image of NGC 6643. From the galaxy image a unsharp mask was subtracted to enhance the contrast of the spiral arms. The Figures show the contours for the simulation with $f_d = 45\,\%$ and corotation radii (red circles) of 6.5 and 8.0 kpc. These two simulations reproduce the galaxy's morphology comparably well. The full set of simulation results is shown in Appendix E.

6.4.2.2. The gas velocity field

The observed gas velocity field of NGC 6643 does not reveal an exceedingly high amount of small scale noise (see Figure 6.22 for three position angles). In the central region the rise of the rotation curve is not particularly steep. As for NGC 5676, the observed data comprise only 7 slit positions, missing one measurement at the 0° position angle.

In Figure 6.22 the comparison of the simulations with the observed data is presented for a sample of three position angles of NGC 6643, illustrating the overall fit quality. Shown are the simulated curves for a near maximal disk case ($f_d = 85\,\%$ in green) and the one for the setup using the most massive halo ($f_d = 20\,\%$ in red). Considering the rather moderate match of the gas density field with the spiral structure, the correspondance of the simulated velocity field of the light disk model with the data is respectably good. Particularly, the global overlap of the curves is striking. From all observed 14 slit positions, given in Appendix E, it can be seen that the comparison turns out very good for the complete velocity field. The simulations fail however, to reproduce a substantial number of the single wiggles pointing towards non-gravitationally induced gas dynamics. This will complicate the conclusion process, which disk mass fraction setup eventually explains the observed gas dynamics best.

The left partition of Figure 6.23 shows the results from the full χ^2-analysis of the runs. As for NGC 3810, the result from the global χ^2-analysis yields a very smooth distribution across the studied parameter space. Accordingly it must be concluded that the amount of non-gravitationally induced gas dynamic wiggles is rather high and probably as abundant as the gravitationally induced ones.

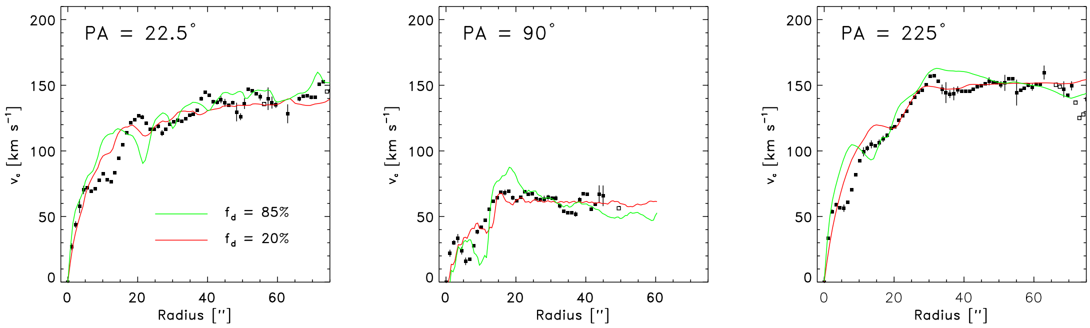

Figure 6.22 Example of the comparison of the simulation results to the observed kinematics of NGC 6643. Velocity field are shown for three position angles. Presented are results from simulations with $f_d = 20$ and 85 %, assuming a pattern rotation $\Omega_p \approx 28.5\,\mathrm{km\,s^{-1}\,kpc^{-1}}$ ($R_{CR} = 6.5$ kpc). Both simulations yield a comparably good match. The full comparison is shown in Appendix E.

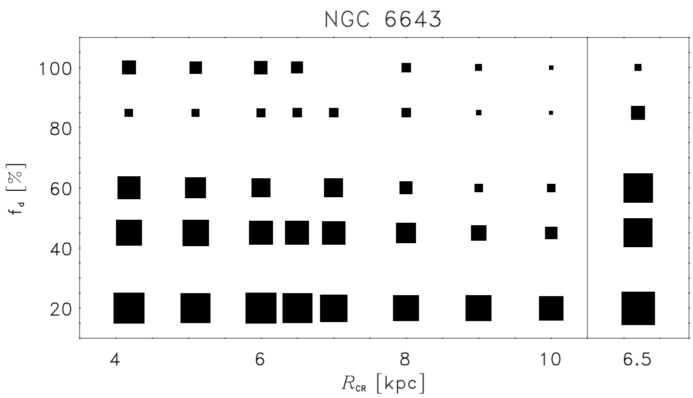

Figure 6.23 Graphical presentation of the global χ^2-analysis of all the velocity simulations for NGC 5676 (left partition). At right, the χ^2-analysis of the reduced data set is shown for a corotation radius $R_{CR} = 6.5$ kpc. Large boxes indicate better χ^2/N agreement between the simulated velocity field and the observed kinematics.

The analysis of only the fraction of the velocity field, for which most likely gravity is the dominant driving force of the gas (see Section 4.3.2.1 for a description of the method) allows slightly more reliable conclusions. As for NGC 3810, slightly more than 50 % of the observed data points have been rejected from the comparison. From the results of the χ^2/N comparison on the reduced data set, displayed in the right partition of Figure 6.23, it can be seen that low and medium disk models provide a comparably good agreement between observations and simulations. This rather vague result comes not unexpected, considering the weak spiral density wave in NGC 6643. If the stellar mass is only poorly concentrated within the spiral arms, the gravitational influence of the arms excerts also weak forcing on the gas. Reproducing these subtle effects with the simulations is difficult. In light of this, the conclusion that a heavy disk scenario is unlikely for NGC 6643 can already be regarded as a respectable success.